Quantitative Hole Mobility Simulation and Validation in Substituted Acenes

Daniel Vong,[†] Tahereh Nematiaram,[‡] Makena A. Dettmann,[†] Tucker L. Murrey,[†] Lucas S. R. Cavalcante,[¶] Sadi M. Gurses,[¶] Dhanya Radhakrishnan,[§] Luke L. Daemen,[‖] John E. Anthony,[⊥] Kristie J. Koski,[§] Coleman X. Kronawitter,[¶] Alessandro Troisi,[‡] and Adam J. Moulé[*,¶]

†*Department of Materials Science and Engineering, University of California Davis, Davis, CA, USA*
‡*Department of Chemistry, University of Liverpool, Liverpool, UK*
¶*Department of Chemical Engineering, University of California Davis, Davis, CA, USA*
§*Department of Chemistry, University of California Davis, Davis, CA, USA*
‖*Oak Ridge National Lab, Oak Ridge, TN, USA*
⊥*University of Kentucky, Lexington, KY, USA*

E-mail: amoule@ucdavis.edu

Methodology

Brillouin scattering measurement

Brillouin scattering was acquired with a 3×3-pass Sandercock scanning tandem Fabry-Perot interferometer (TFP-1) with a Coherent Verdi V6 Nd:YVO4 laser (λ_0 = 532.15 nm). The laser was focused onto the TIPS-Pentacene crystal with ∼10-15 mW power and with acquisition times from 8-24 hours per spectrum. The mirror spacing of the etalons was 3 mm (90R) or 6 mm (180) with a scan rate of 550 giving an effective spectral window of 50 GHz and 25 GHz, respectively. The narrower spectral window was displayed in Figure 1 in the main text. No other peaks were found at higher frequencies, which indicates that this measurement captured the principle acoustic phonon modes, the translational modes along the molecule's axes. Entrance pinholes were at 450 μm with an exit pinhole of 700 μm providing an overall system finesse of 70 (180) to 140 (90R). Brillouin scattering spectra were not simulated using DFT given the computational expense associated with a box size of 1000's of molecules.

Brillouin scattering measurements of TIPS-Pentacene (Fig. S1) was acquired in two geometries with respect to the crystalline axis. The 180° (black curve) geometry observes the directly reflected signal while the 90° (red curve) geometry observes a signal reflected to an angle of 90°. On a fundamental level, Brillouin scattering results from the interaction of a photon with the acoustic phonons of a material on the mesoscopic scale (∼0 to a few cm^{-1}).[1] Thus the principal acoustic phonons that produce the largest molecular displacement are measured directly using Brillouin scattering. A Brillouin spectrum has a single elastically scattered component, which is blocked in these measurements by a shutter, surrounded by Stokes and Anti-Stokes scattering peaks. Each peak consists of one longitudinal or quasi-longitudinal phonon mode, and depending on the geometry and symmetry of the measurement, one or two quasi-transverse acoustic modes. These measurements each show only one longitudinal or quasi-longitudinal mode. The Brillouin frequency shift ($\Delta\nu$) is related to the acoustic sound velocities, V by:

$$\Delta\nu(Hz) = \pm\frac{2nV}{\lambda_o}\sin\frac{\theta}{2} \tag{1}$$

where n is the refractive index, θ is the scattering angle as measured inside the sample, and λ_0 is the free-space wavelength of the laser. The geometries of 180° and 90° measure the same sound velocities, thus we can determine n by the frequency shift from both measurements:

$$n = \left(\frac{1}{\sqrt{2}}\right)\left(1-\left(\frac{\nu_{90r}}{\nu_{180}}\right)^2\right)^{-1/2} \tag{2}$$

The Brillouin frequency shift in 180° is 12.90 +/- 0.1 GHz. Sound velocities from these measurements of TIPS-Pentacene show 2451 m/s. Assuming a density of 1.10 g/cm^3, this gives a stiffness of c_{11} = 6.61 GPa as calculated from:

$$V_L = \sqrt{\frac{c_{11}}{\rho}} \tag{3}$$

Converting from a frequency scale to an energy scale shows that the principal acoustic phonon in TIPS-Pentacene corresponds to ~50 μeV or 0.43 cm^{-1}. Notably, this energy is at least an order of magnitude below the phonon energies measured by INS, FTIR, Raman or Terahertz spectroscopies. This acoustic phonon mode has the lowest energy, longest wavelength, and largest displacement of any phonon mode. Therefore, this phonon mode is the most likely molecular motion to be measured using diffuse scattering techniques, and the principal acoustic phonon cannot be measured using Terahertz spectroscopy with energy above 20 cm^{-1}.[2] The motions of the acoustic phonon modes measured using Brillouin scattering are much slower than the charge hopping events in OSCs and therefore do not contribute to off-diagonal σ or reduce μ_h. Brillouin scattering measured on Rubrene[3] show multiple acoustic modes while Rubrene has measured μ_h >10 cm^2/Vs. Despite any detrimental actions of these modes, high μ_h is retained.

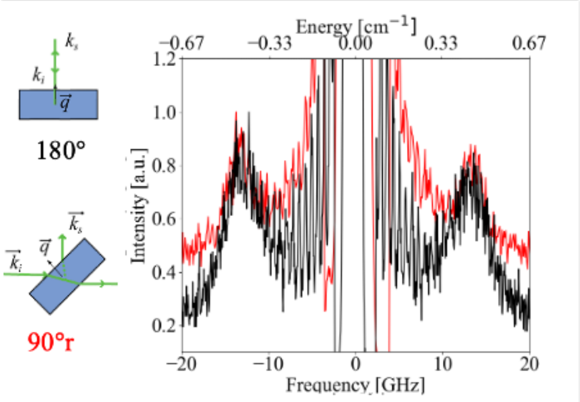

Figure S1: Brillouin scattering in 180° (top left, black spectrum) and 90°r (bottom left, red spectrum) scattering geometries. Only one longitudinal acoustic mode is observed. Details are given in the manuscript.

INS, Raman, and FTIR measurement and modeling

Inelastic neutron scattering spectrum was measured using the VISION spectrometer at the Spallation Neutron Source at Oak Ridge National Laboratory (ORNL). VISION samples were loaded in vanadium sample holders inside a dry helium glove box. An empty sample holder was measured and subtracted from the measured spectra. All data sets were collected at 5K.

A Bruker VERTEX 70 FTIR spectrometer equipped with a liquid nitrogen cooled MCT detector was used to collect reflectance FTIR spectra on powdered TIPS-Pentacene. The sample was placed in a multi-reflection ATR crystal (ZnSe) with a Specac's Gateway ATR accessory set to an incidence angle of 45 degrees. The spectrum represents the average of 128 scans.

Computed inelastic neutron scattering spectra were produced similar to our previously developed plane-wave density functional theory model as implemented in VASP[4,5] with PAW pseudopotentials,[6] with a decrease of the maximum force criteria for the ionic relaxation loop to 0.002 eV/Å and the electronic energy converged to 10^{-8} eV. The optPBE[7,8] functional was used in describing the exchange-correlation along with the non-local vdW[9] correlation functional for dispersion interactions. The basis set plane wave energy cutoff was increased to 800 eV, with a 4×4×2 Γ-centered k-point mesh for the substituted acenes, and 2×3×2, 3×2×1, and 2×2×2 k-point mesh for BTBT, C8-BTBT, and Rubrene, respectively. The crystallography files used in the computation are found in Refs. 10–14. Phonopy[15] was used to calculate the vibrational modes and energies on a 2×2×1 supercell for the substituted acenes, and 1×2×2 ,2×2×1, and 1×1×1 for BTBT, C8-BTBT, and Rubrene, respectively, using the finite displacement method (more in the next subsection), wherein symmetry inequivalent atoms are displaced by 0.001 Å and restoring forces are calculated. The supercell sizes ensure a minimum of 10 Å per crystallographic length and 4 molecules per supercell, which we have found is necessary to converge the calculation. The INS spectrum was produced using the energies and forces from DFT using the oCLIMAX[16] tool provided by Oak Ridge National Laboratory. oCLIMAX inputs specific geometry considerations based on the VISION beam line. Phonon k-points in Phonopy were increased until INS spectral convergence was reached.

Γ-point phonon eigenvectors and frequencies and Born effective-charge tensors were calculated in VASP using the same parameters listed in the INS model. The DFT calculated[17] off-resonant isotropic Raman intensities were calculated using the Python program developed by Fonari and Stauffer.[18] FTIR intensities were calculated using the Phonopy-Spectroscopy methodology by Skelton.[19]

Finite displacement supercell

Here we describe the finite displacement supercell method in a simplified 2D convention to obtain inputs to the scattering law. Using Phonopy, finite displacement is a method to obtain the phonon eigenvectors (phonon displacement vectors) and eigenvalues (phonon frequencies) beyond the Γ-point (as some DFT packages are limited to Γ-point phonons or can only handle smaller systems). A supercell with cell dimensions >10 Å in each crystallographic direction of the relaxed primitive cell is created and a displaced atom from its equilibrium position induces a force on every other atom (large enough cell to minimize the chance of the displaced atom self-interaction, small enough displacement to stay in the harmonic regime), and can be systematically applied to every other symmetry in-equivalent atoms to obtain a matrix of pairwise force constants,

$$\Phi_{nimj} = \frac{\partial F_{ni}}{\partial u_{mj}} \tag{4}$$

where F is the force, u is the displacement, subscripts n and m are atom labels, and i and j are Cartesian directions. The mass weighted Fourier transform of the force constant matrix,

$$\tilde{D} = \frac{\Phi_{nimj}}{\sqrt{m_n m_m}} e^{i\vec{q}\cdot(r_{mj}-r_{ni})} \tag{5}$$

is defined as the dynamical matrix, where m are the atom masses. Diagonalizing the dynamical matrix gives the solutions to the harmonic approximation's eigenvalue problem, specifically the square of the vibrational mode frequencies and atomic displacements,

$$[\tilde{D}][\varphi] = \omega^2[\varphi] \tag{6}$$

The solutions to the eigenvalue problem are inputs to OCLIMAX,[16] a proprietary software written by the VISION vibrational neutron spectrometer beamline scientists at Oak Ridge National Lab, which reproduces spectra with the instrument sensitivity and spectral response of VISION, given by

$$S(Q, n\omega_s) = \frac{Q \cdot U_s^{2n}}{n!} e^{-Q\cdot U_{total}^2} \quad U_s = \sqrt{\frac{\hbar}{2m\omega_s}}\varphi_s \tag{7}$$

which is the reduced form of the scattering law for low temperature, hydrogen containing materials, where n is the population of phonon mode s, and Q is the neutron momentum transfer.

Dynamic disorder and mobility

The methodology and computational detail(s) are identical to those presented in Ref. 20 except for the calculation of the phonons. Briefly, the following standard Hamiltonian is used,

$$\begin{aligned}\hat{H} = \\ &\sum_{i} \epsilon_i \hat{c}_i^{+} \hat{c}_i + \sum_{<ij>} J_{ij}^{0} \hat{c}_i^{+} \hat{c}_j + \sum_{M} \hbar\omega_M (\hat{a}_M^{+} \hat{a}_M + \frac{1}{2}) + \\ &\sum_{i,M} g_{i,M} \frac{1}{\sqrt{2}} (\hat{a}_M^{+} + \hat{a}_M) \hat{c}_i^{+} \hat{c}_i + \sum_{i \neq j, M} g_{ij,M} \frac{1}{\sqrt{2}} (\hat{a}_M^{+} + \hat{a}_M) \hat{c}_i^{+} \hat{c}_j .\end{aligned}$$

The first two terms indicate the electronic part of the Hamiltonian, the third term describes the lattice phonons, and the last two terms describe the local and non-local electron-phonon couplings. ϵ_i denotes the on-site electronic energy of the hole; J_{ij}^0 is the transfer integral between adjacent molecules at the equilibrium geometry; $\hbar\omega_M$ and $k_B T$ are the phonons and the thermal energies, respectively; $\hat{c}_i^{+}(\hat{c}_i)$ are the creation (annihilation) operators for a hole at site i (there is one state per site); $< ij >$ is the nearest-neighbour pairs of occupied sites; $\hbar$ is the reduced Planck constant; ω_M is the phonon frequency of mode M; $g_{i,M}$ and $g_{ij,M}$ are the local and non-local electron-phonon couplings measuring the strength of interaction between charge carrier and intra-molecular and inter-molecular vibrations; and $\hat{a}_M^{+}(\hat{a}_M)$ are the phonon creation (annihilation) operators, respectively. The local electron-phonon coupling causes the modulation of the site energies (i.e. local dynamic disorder) while the non-local term leads to the fluctuation of the transfer integral, which is typically of the same order of magnitude as the transfer integral itself (i.e. non-local dynamic disorder).[21] We computed the transfer integral using the below equation,

$$J_{ij} =< \varphi_i | \hat{F} | \varphi_j > \tag{8}$$

where φ_i and φ_j are the localized highest-occupied molecular orbital (HOMO) of molecule i and j, respectively, and $\hat{F}$ stands for the Fock operator of the dimer system. Calculations of the transfer integrals are carried out based on *ab initio* methods at the B3LYP/3-21g* level of the theory as implemented in Gaussian16.[22] The sign of J_{ij} will depend on the phases of φ_i and φ_j, being negative if the signs of the overlapping wavefunctions are opposite, and positive if the signs are alike. The local electron-phonon coupling is computed using the nuclear displacement between equilibrium positions before and after the charge transfer, as explained in Refs. 23 & 24.

To consider the impact of local electron-phonon coupling on the mobility, we defined an energy cut-off ($2k_BT$) to consider the local electron-phonon coupling classically; all the local modes above this cut-off (i.e. $\hbar\omega_M \geq 2k_BT$) contribute to the calculation of a renormalization factor f as explained in Ref. 25 and defined as $f{=}exp(-\sum_M (g_{i,M}/\hbar\omega_M)^2(2N_M+1))$ where $(g_{i,M}/\hbar\omega_M)$ is the dimensionless Huang-Rhys factor[26] or the local electron-phonon coupling for nuclear mode M of frequency ω_M and $N_M = (exp(\hbar\omega_M/K_BT) - 1)^{-1}$ stands for the occupation number. T was set to 300 K and all the modes below this cut-off (i.e. $\hbar\omega_M < 2k_BT$) contribute to the on-site energy fluctuations $\sigma_{local} = \sqrt{\lambda_S k_B T}$ where $\lambda_S = \sum_M g_{i,M}^2/\hbar\omega_M$ contains contributions only from low-frequency modes.

The non-local electron-phonon coupling $g_{ij,M}$ is a measure of how the transfer integral between molecular pair i and j is modulated by a displacement along a phonon mode M and can be expressed as below,[27] where ∇J_{ij} is the gradient of the transfer integral with respect to the atomic dispalcement and Q_M is the vector that denotes the Cartesian displacements of mode M,[28]

$$g_{ij,M} = \nabla J_{ij} Q_M \tag{9}$$

This coupling gives access to the non-local dynamic disorder σ_{ij} a global measure of the fluctuations of the transfer integrals J_{ij} when compared with their average values,[29]

$$\sigma_{ij}^2 = \frac{1}{N}\sum_M \frac{|g_{ij}^M|^2}{2} coth(\frac{\hbar\omega_M}{2k_B T}) \tag{10}$$

With N being the number of points employed to sample the q-space.

TLT[30] is used to evaluate the mobility as it has proved able to produce results in agreement with more complicated quantum dynamics propagation schemes[31,32] as well as experimental measurements.[27] According to this theory, the effects of dynamic disorder can be monitored by a transient localization over a length L within a fluctuation time scale given by the inverse of the typical intermolecular oscillation frequency $\tau \sim 1/\omega_0$. In this work, τ is set to 0.13 ps, wherein it was concluded in Ref. 33 that τ does not change much between molecules, and that as $\mu \propto L_\tau^2/\tau$, L_τ^2 increasing with fluctuation time results in a weak dependence of τ on μ_h for the substituted acenes tested. The charge mobility in this theory is expressed as,

$$\mu = \frac{e}{k_B T}\frac{L^2}{2\tau} \tag{11}$$

where e is the electron charge, and L is computed as shown in Ref. 27. We use the exact diagonalization method proposed in Ref. 34 to calculate the squared transient localization length in the crystal's high-mobility plane. Furthermore, in the present study, the generalized form of transient localization theory, as described in Ref. 20, is utilized to consider the impact of local electron-phonon coupling in addition to non-local electron-phonon term. As such, an additional on-site gaussian fluctuation σ_{local} (as defined above) is considered which takes into account the impact of low-frequency modes and the transfer integrals and their fluctuations are scaled by the renormalization factor f which considers the high-frequency vibrations.

In contrast to hopping theory, which calculates an incorrect temperature dependence for mobility, or band theory, which calculates nonphysical scattering lengths,[31,33] TLT demonstrates accurate prediction of charge mobility given fully converged vibrational calculations. Thus, accurate predictions of μ_h allow for potential molecular designs to be rapidly screened and provide insight into high μ design rules. The key reason for selecting this model, is that it connects in a transparent way the vibrational properties, electronic structure, and μ. It is therefore easy within this theory to disentangle the different sources of errors in computing the phonons.

Rubrene partial mode analysis

Rubrene is much less structurally identical than the acenes discussed in this letter, making a direct comparison across similar motions at similar energies impossible. Nevertheless, Rubrene has the highest μ_h of any OSMs, warranting a partial node analysis. The dominant feature at low energy in Fig. S11a ($\sim$30 cm^{-1}) is comprised of multiple phonons, and we highlight the significant modes for Rubrene shown in Figure S14. Rubrene, like C8-BTBT, has opposing axial translation contributing to σ in Figs. S14a and S14b, wherein the phenyl rings reduce the amplitude of axial translation motions. At increasing energies, the weak C–C single bonds connecting the phenyl rings to the tetracene core allow large displacements with complex motions in the phenyl rings, including twisting and flapping, Figs. S14c-e. This in turn elicits an opposing motion from the core resulting in its own twisting, bowing, and other motions.

Supplemental Figures

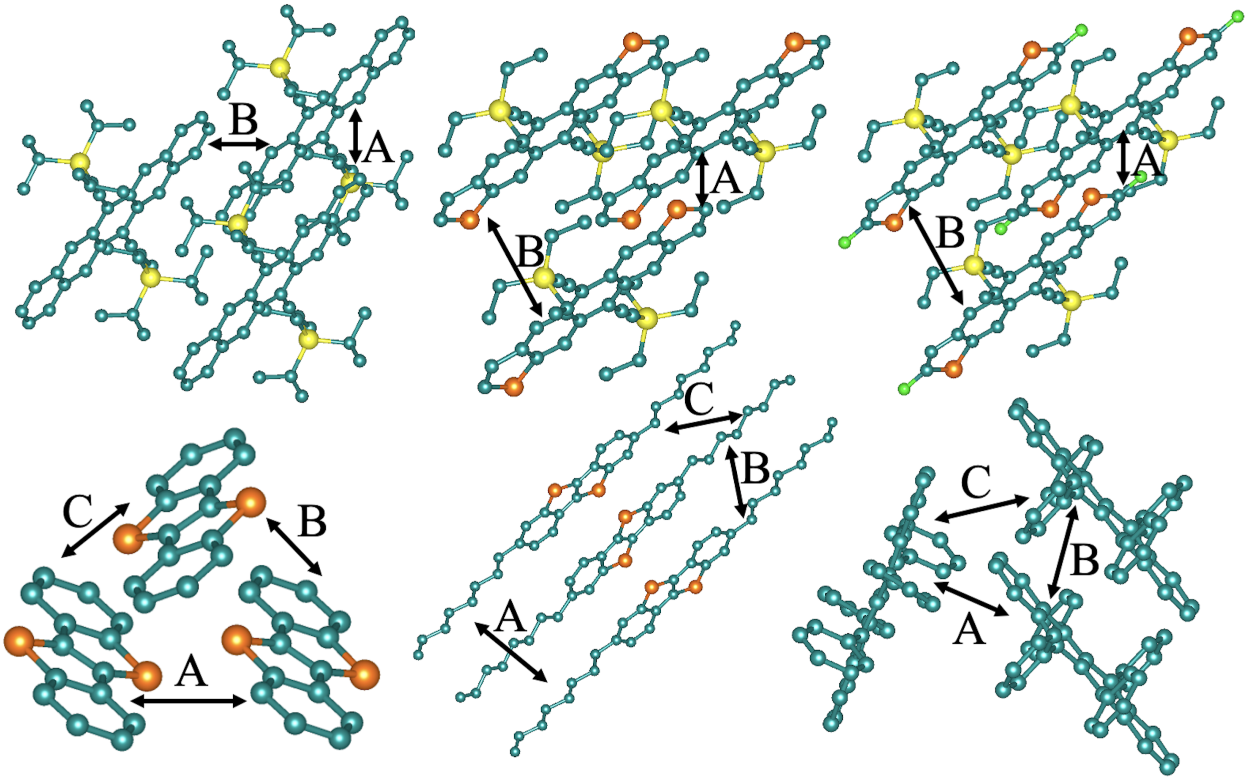

Figure S2: The materials used for this work. From top-left to bottom-right: TIPS-PN, TESADT, diF-TESADT, BTBT, C8-BTBT, and Rubrene. A, B, and C denote the unique molecular pairs in which transfer integrals are computed. Hydrogen atoms have been omitted for clarity.

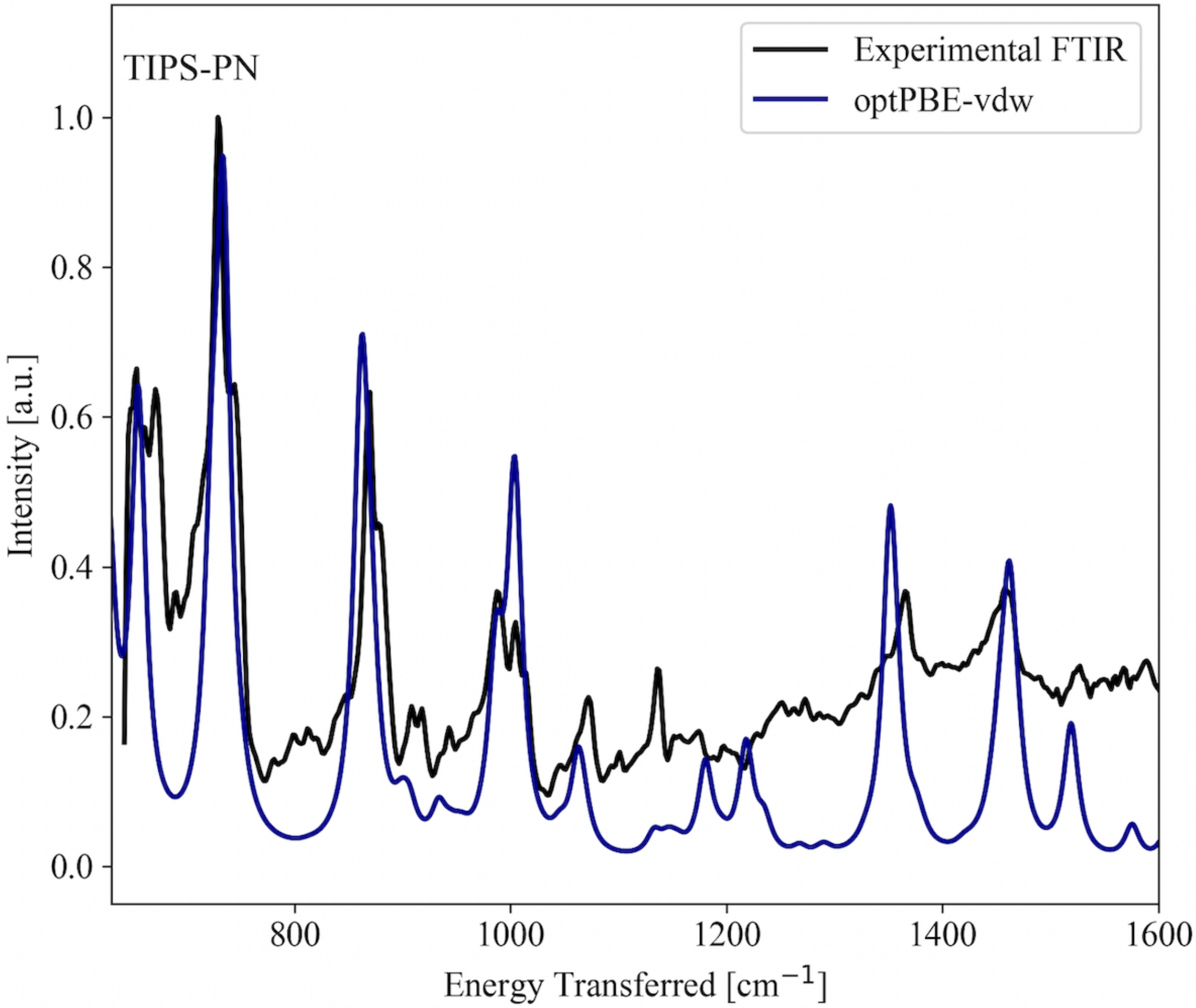

Figure S3: Comparison of experimental (black) and computed optPBE-vdw (blue) FTIR spectra for TIPS-Pentacene. Energy range from 630-1600 cm^{-1}.

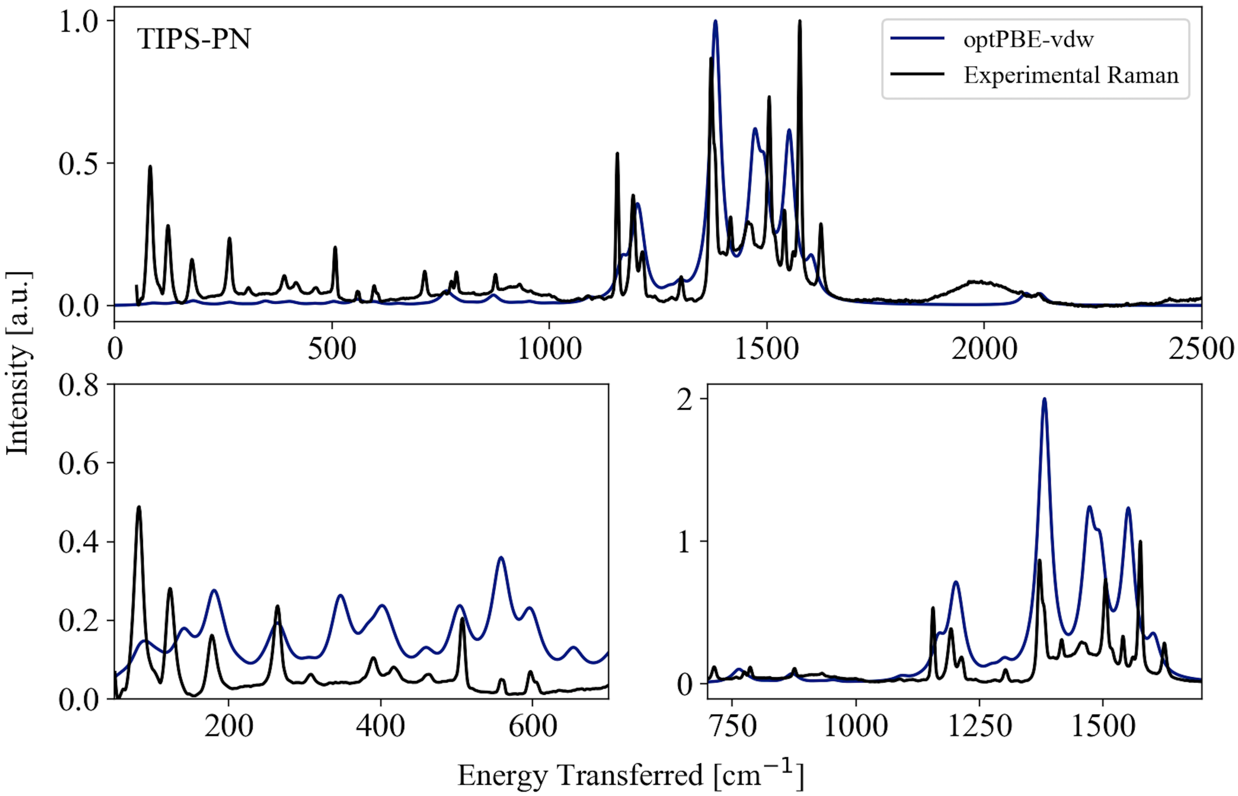

Figure S4: Comparison of experimental (black) and computed optPBE-vdw (blue) Raman spectra for TIPS-Pentacene. Top spectra include energy range from 0-2500 cm^{-1}. Bottom show zoomed-in and scaled spectra for energies 50-700 cm^{-1} (bottom left) and 700-1800 cm^{-1} (bottom right).

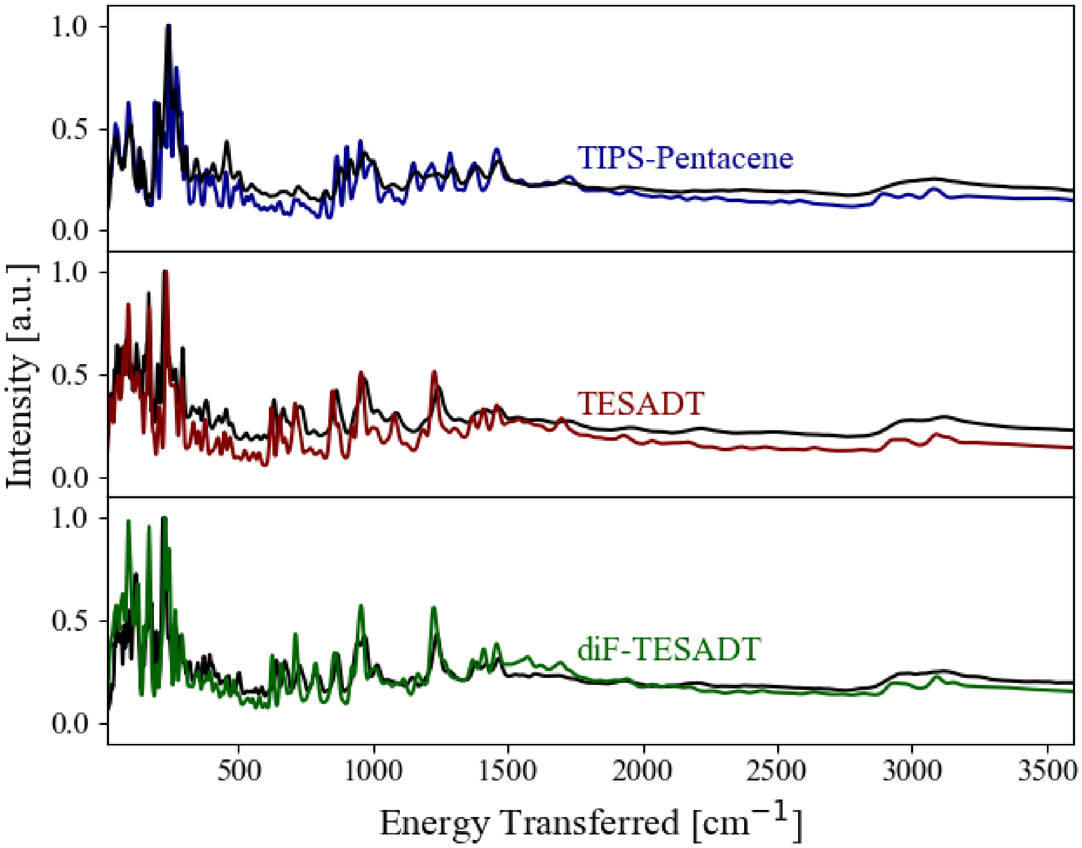

Figure S5: Comparison of experimental (black) and computed optpbe-vdw INS spectra for TIPS-Pentacene (blue), TESADT (maroon), and diFTESADT (green) from 10-3400 cm^{-1}.

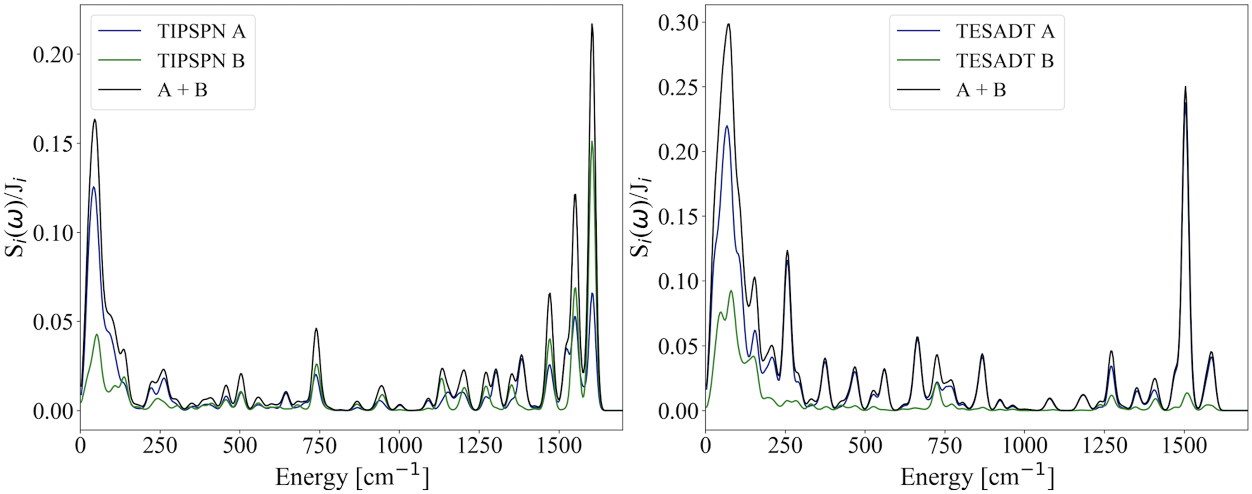

Figure S6: Accumulative spectral density of electron-phonon coupling in the high mobility plane normalized by the transfer integral for TIPS-Pentacene and TESADT. Subscript i denotes the unique molecular pairs A and B.

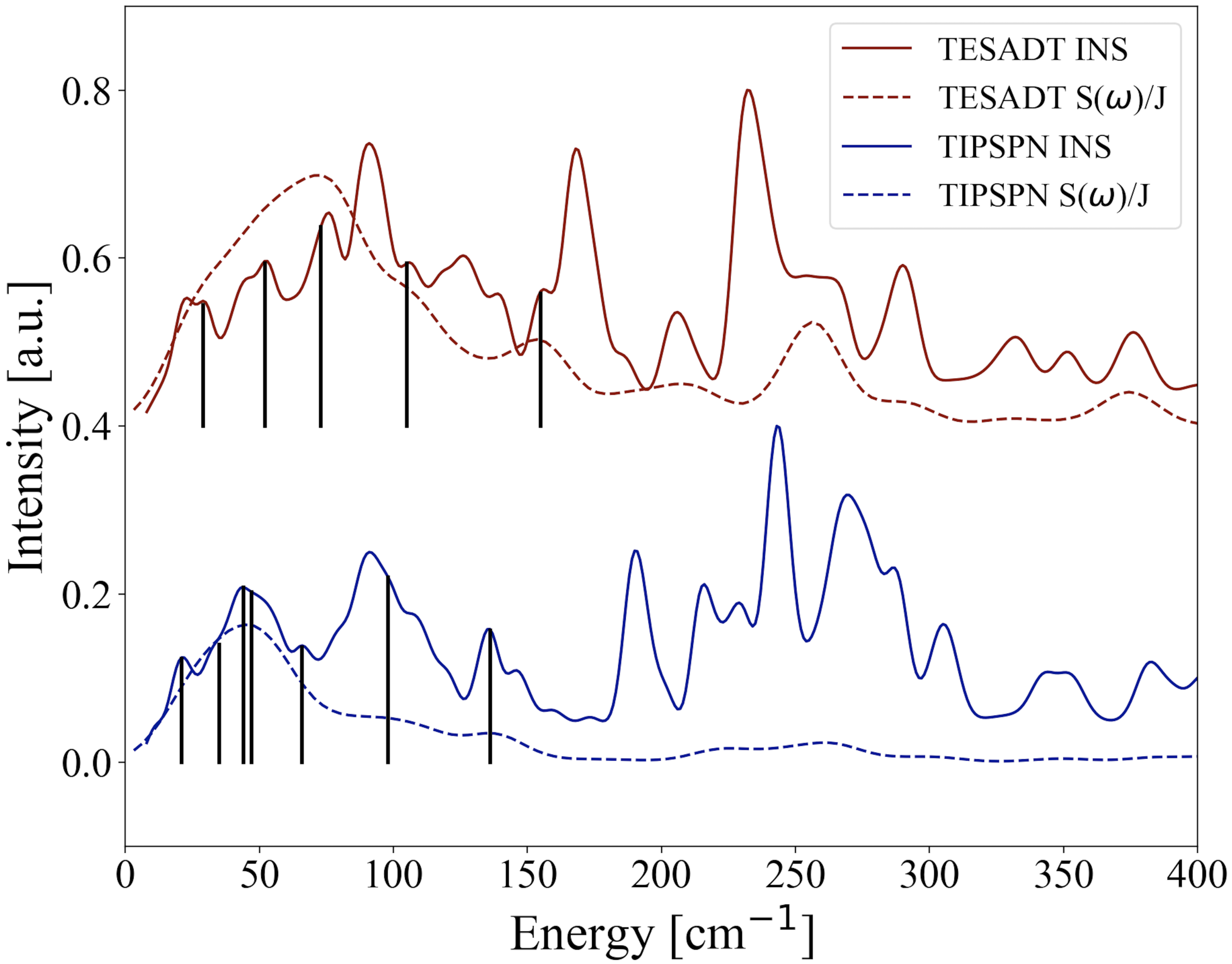

Figure S7: Normalized spectral density of electron-phonon coupling with respective inelastic neutron scattering for TIPS-Pentacene and TESADT. Black vertical lines highlight the phonon modes shown in Figs. S6 and S7 for TIPS-Pentacene and TESADT, respectively.

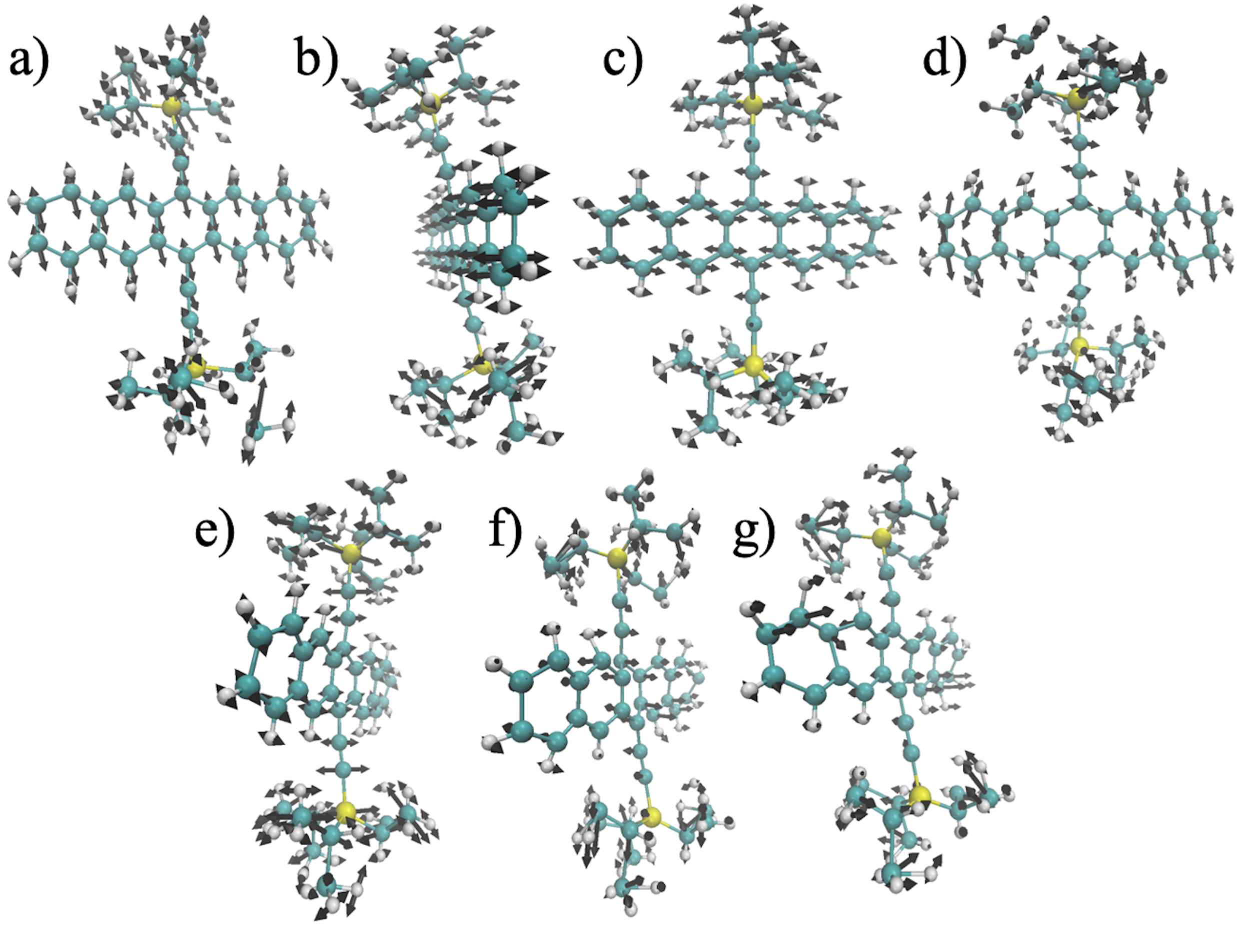

Figure S8: Phonon modes for TIPS-Pentacene in the low energy region with large contribution to σ. Phonon frequencies in wavenumbers are 21, 35, 44, 47, 66, 98, and 136 in for a-g, respectively. Phonons are shown on one molecule included in the primitive unit cell.

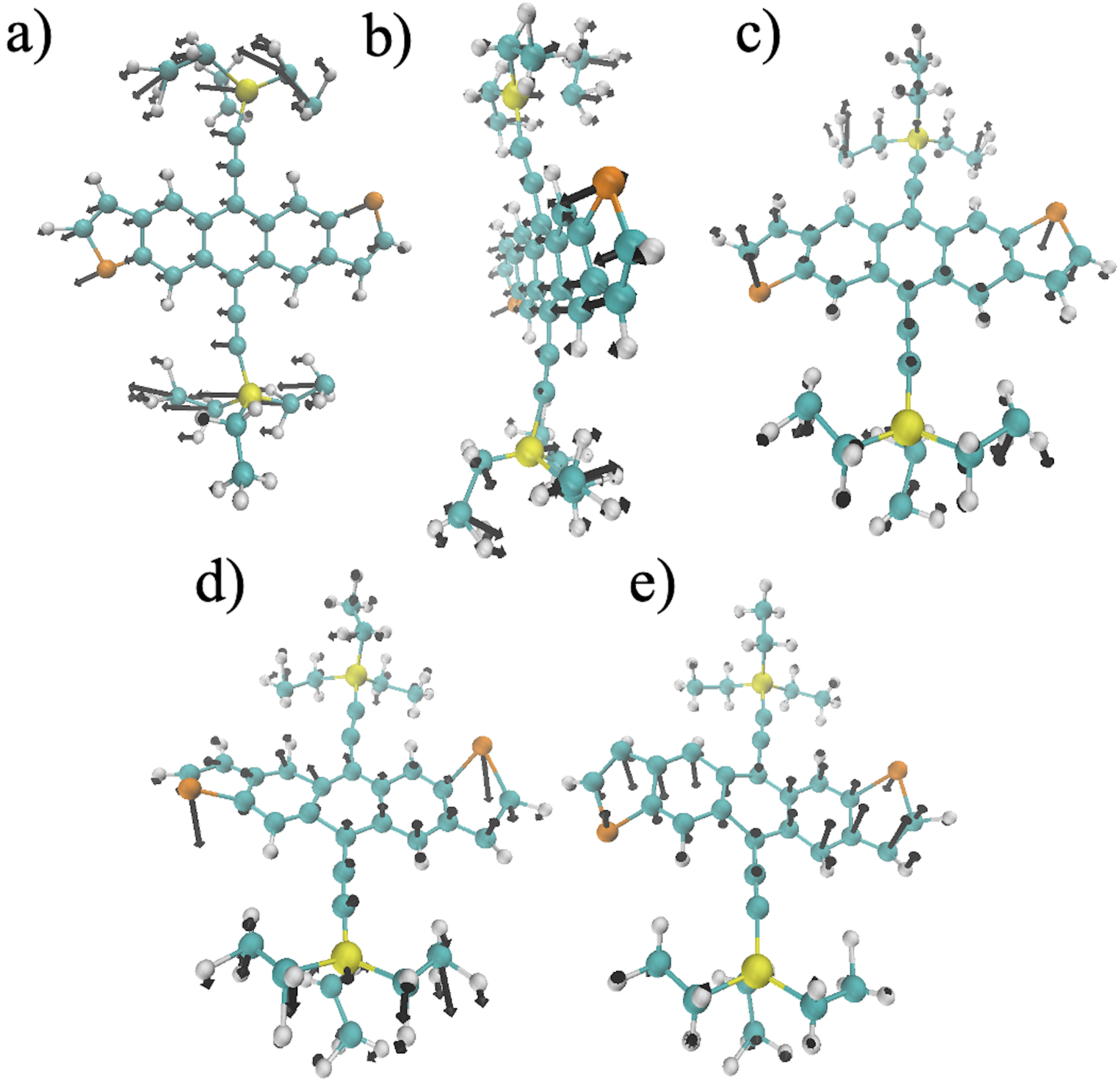

Figure S9: Phonon modes for TESADT in the low energy region with large contribution to σ. Phonon frequencies in wavenumbers are 29, 52, 73, 105, and 155 in for a-e, respectively. Phonons are shown on one molecule included in the primitive unit cell.

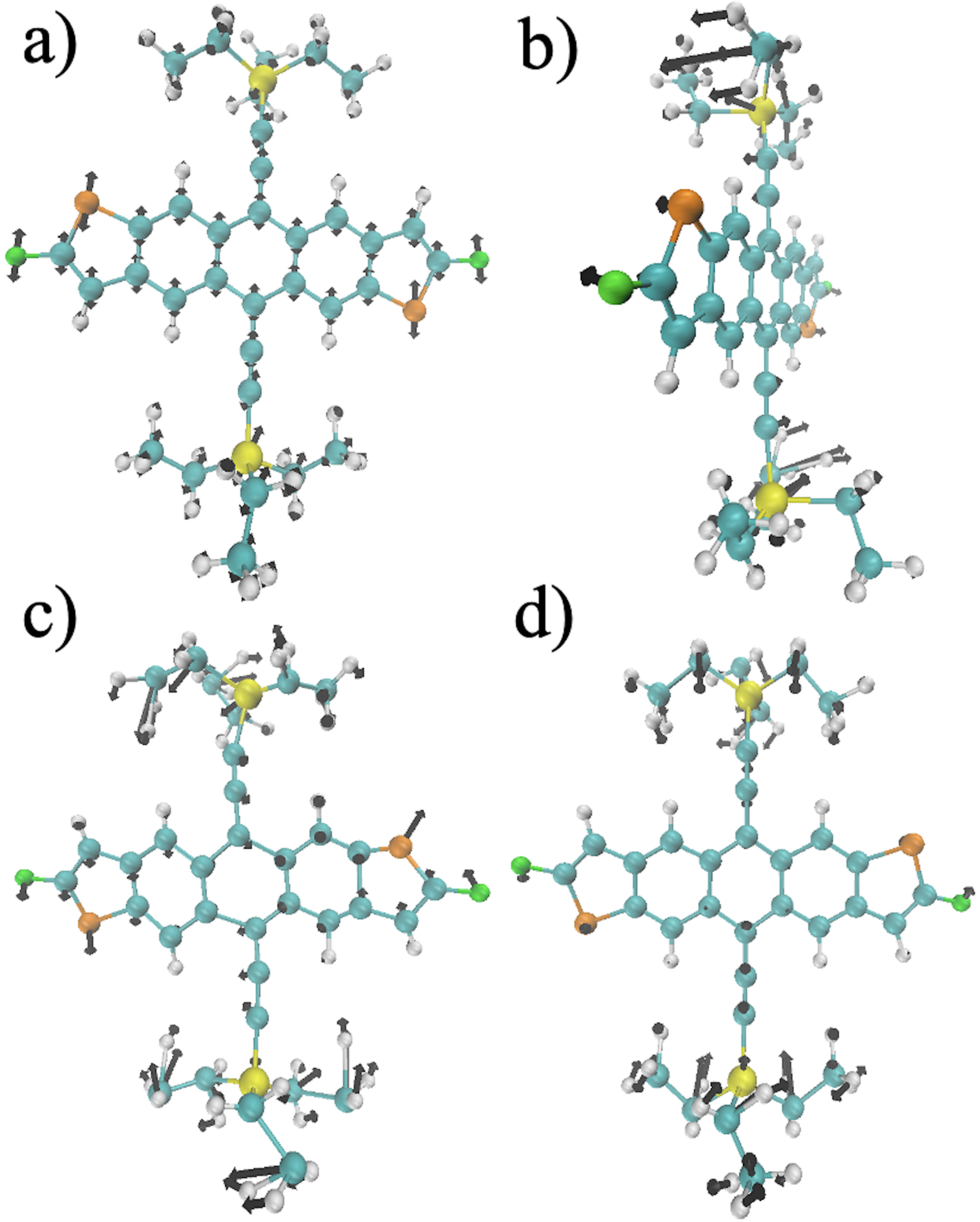

Figure S10: Phonon modes for diF-TESADT wherein the modes of the former unfluorinated analogue had high σ. Phonon frequencies in wavenumbers are 27, 48, 70, and 150 in for a-d, respectively. Phonons are shown on one molecule included in the primitive unit cell.

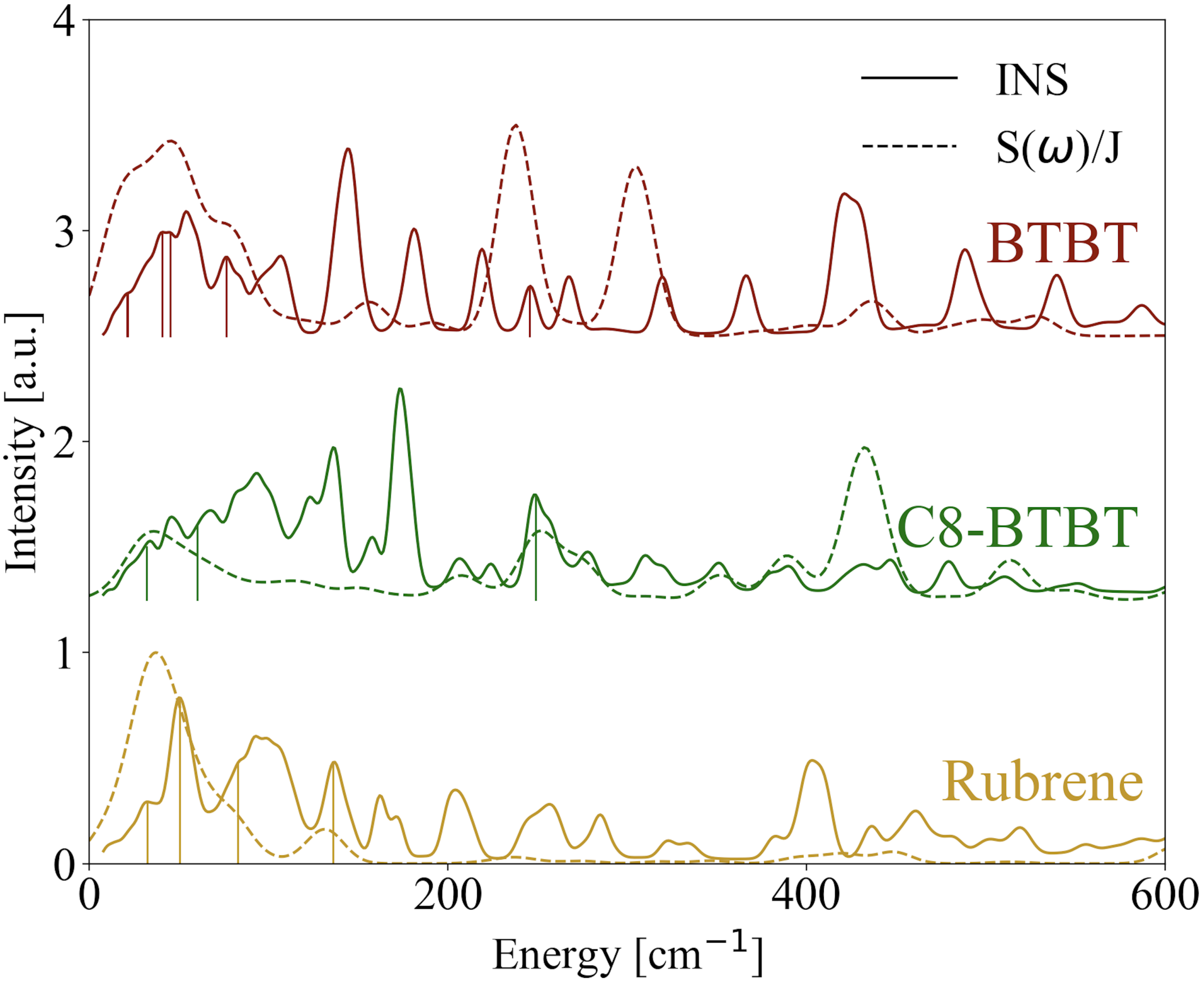

Figure S11: Normalized spectral density of electron-phonon coupling with respective inelastic neutron scattering for BTBT, C8-BTBT, and Rubrene. Vertical lines highlight the phonon modes shown in Figs. S12-S14 for respective molecules.

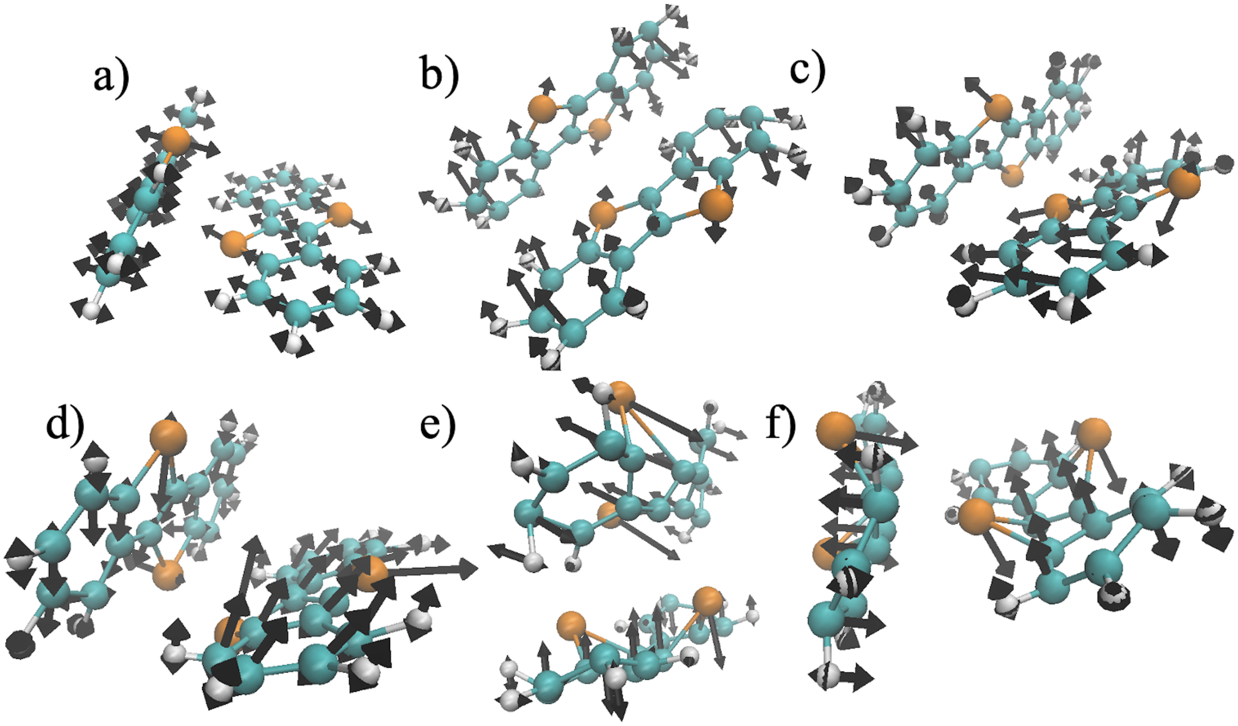

Figure S12: Phonon modes for BTBT in the low energy region with large contribution to σ. Phonon frequencies in wavenumbers are 21.2, 21.5, 40.8, 45.0, 142.2, and 245.6 for a-f, respectively. Phonons are shown on the two molecules included in the primitive unit cell.

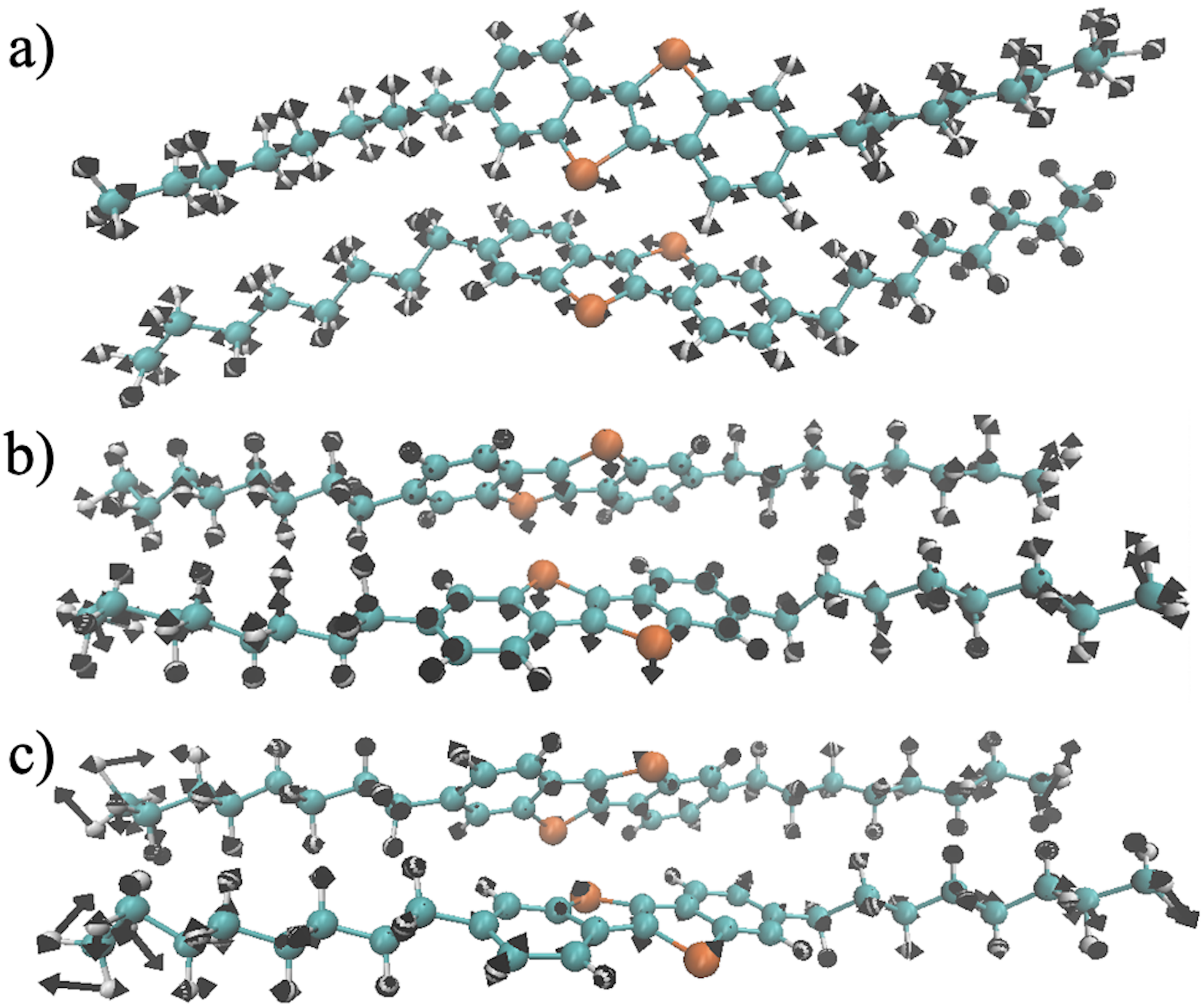

Figure S13: Phonon modes for C8-BTBT in the low energy region with large contribution to σ relative to BTBT. Phonon frequencies in wavenumbers are 32.0, 60.2, and 260.2 for a-c, respectively. Phonons are shown on the two molecules included in the primitive unit cell.

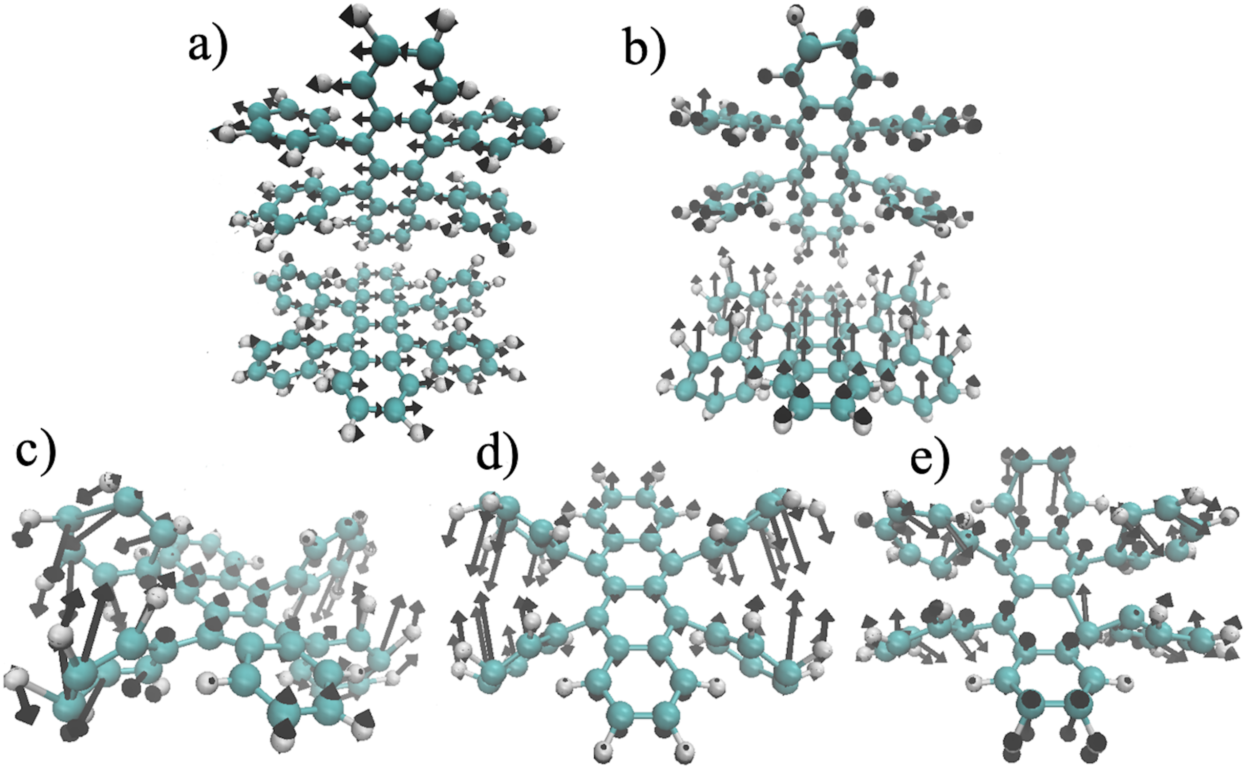

Figure S14: Phonon modes for rubrene in the low energy region with large contribution to σ. Phonon frequencies in wavenumbers are 32.50, 32.54, 50.5, 105.2, and 144.5 for a-e, respectively. Relevant phonons are shown on reduced number of molecules for clarity.

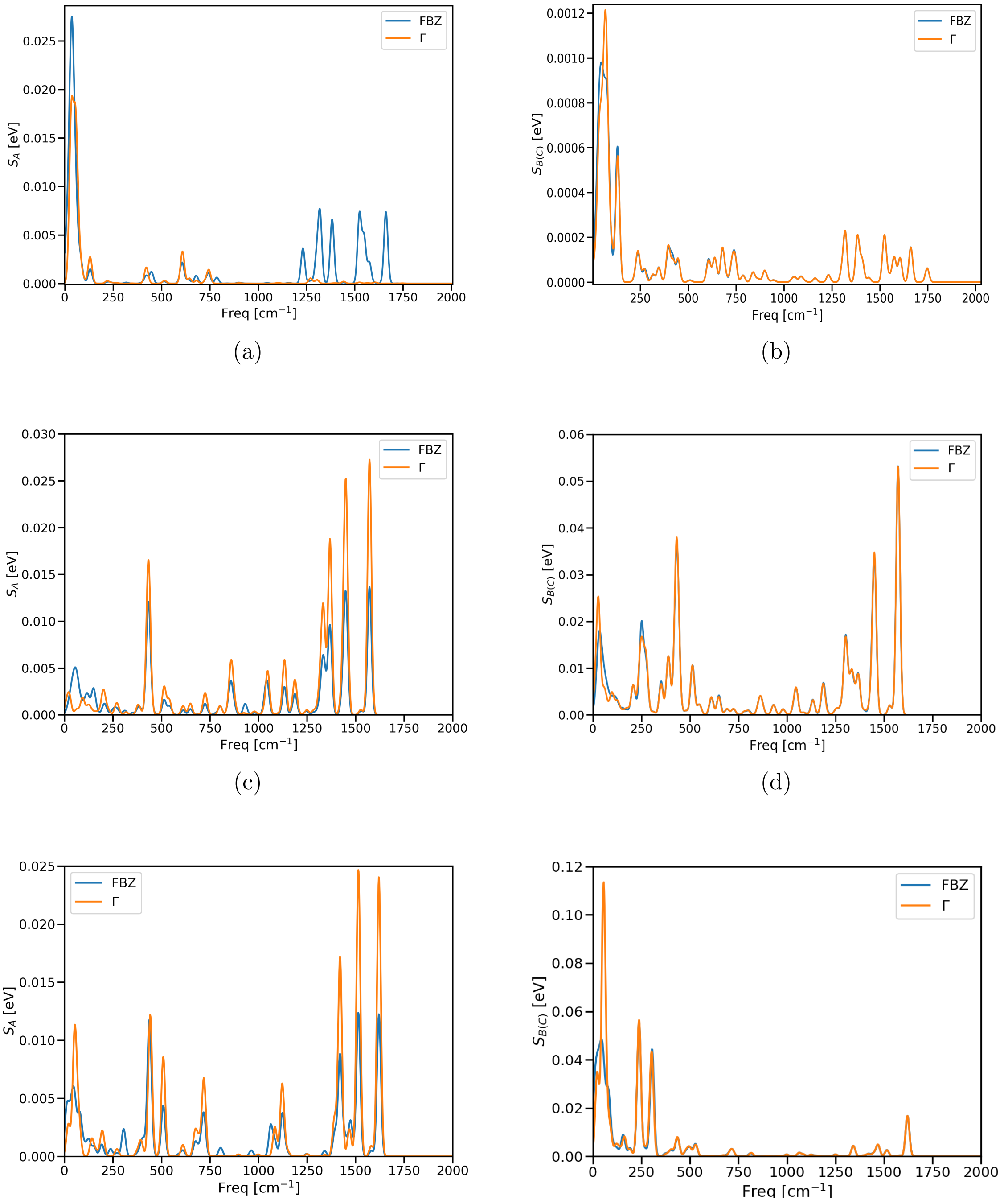

(a) (b)

(c) (d)

(e) (f)

Figure S15: The spectral density of dimers A and B(C) for the considered three molecules, from top to bottom (a-b) Rubrene, (c-d) C8-BTBT and (e-f) BTBT.

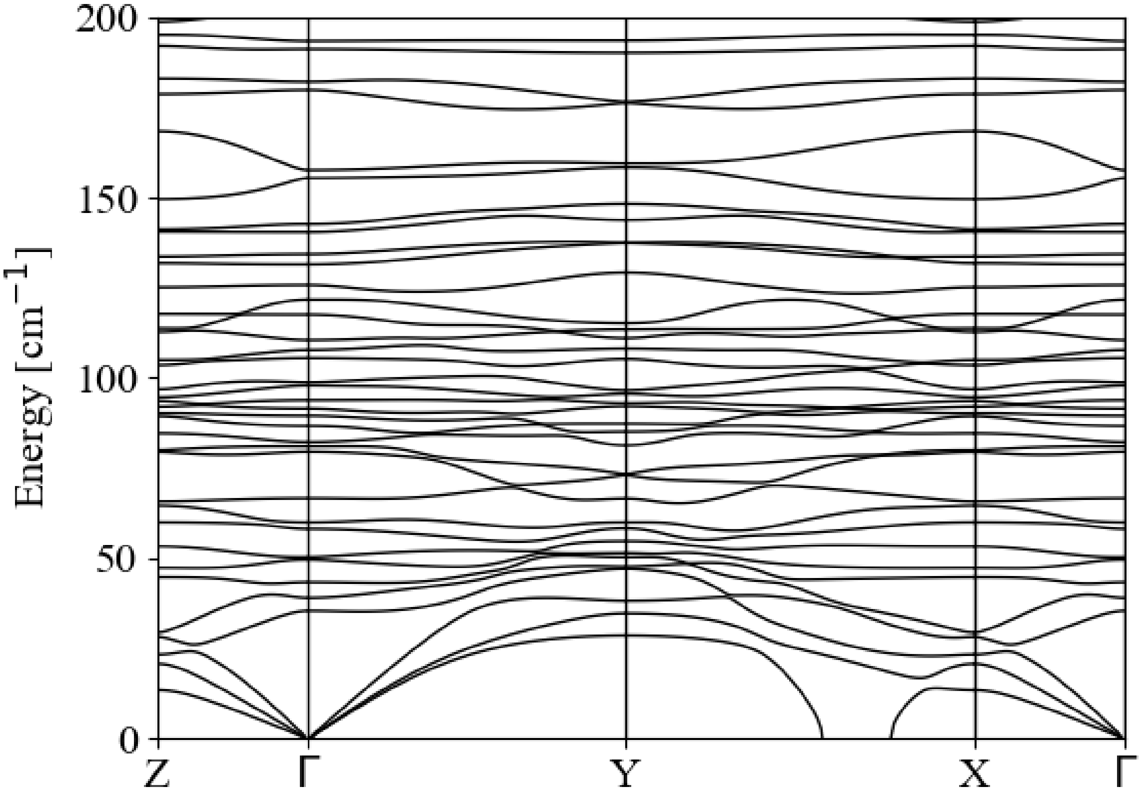

Figure S16: Phonon band structure for TIPS-Pentacene.

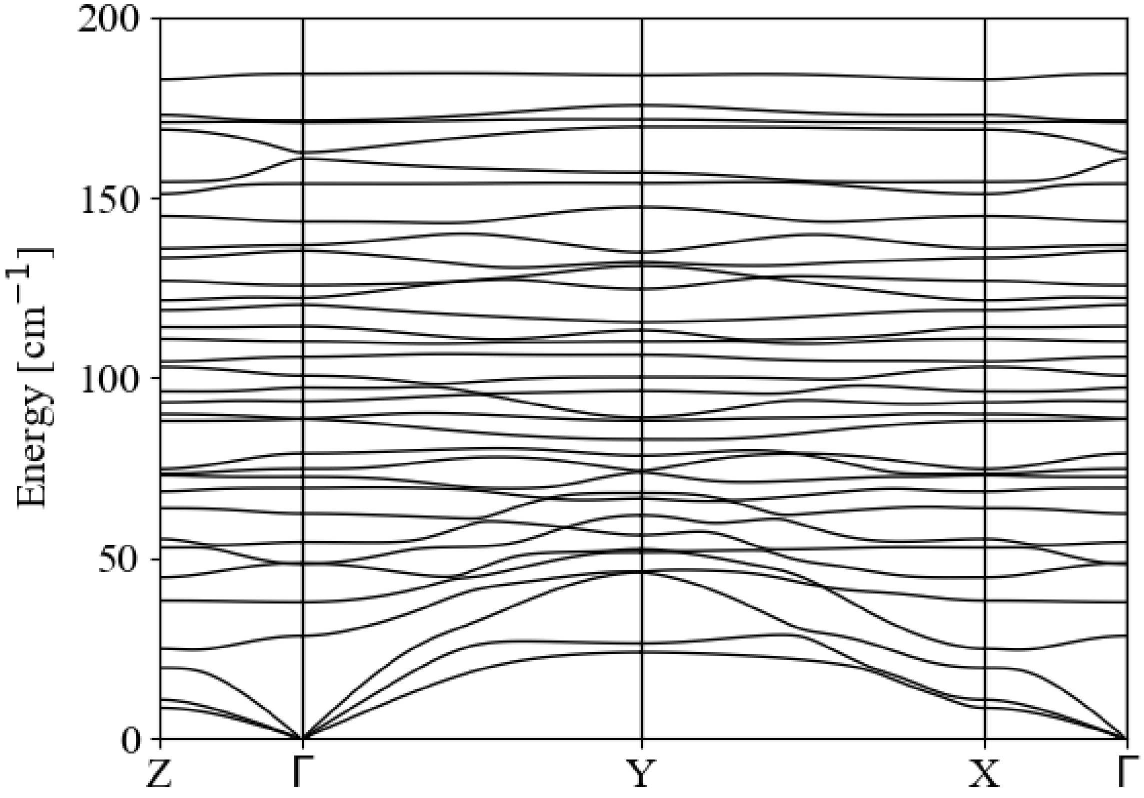

Figure S17: Phonon band structure for TESADT.

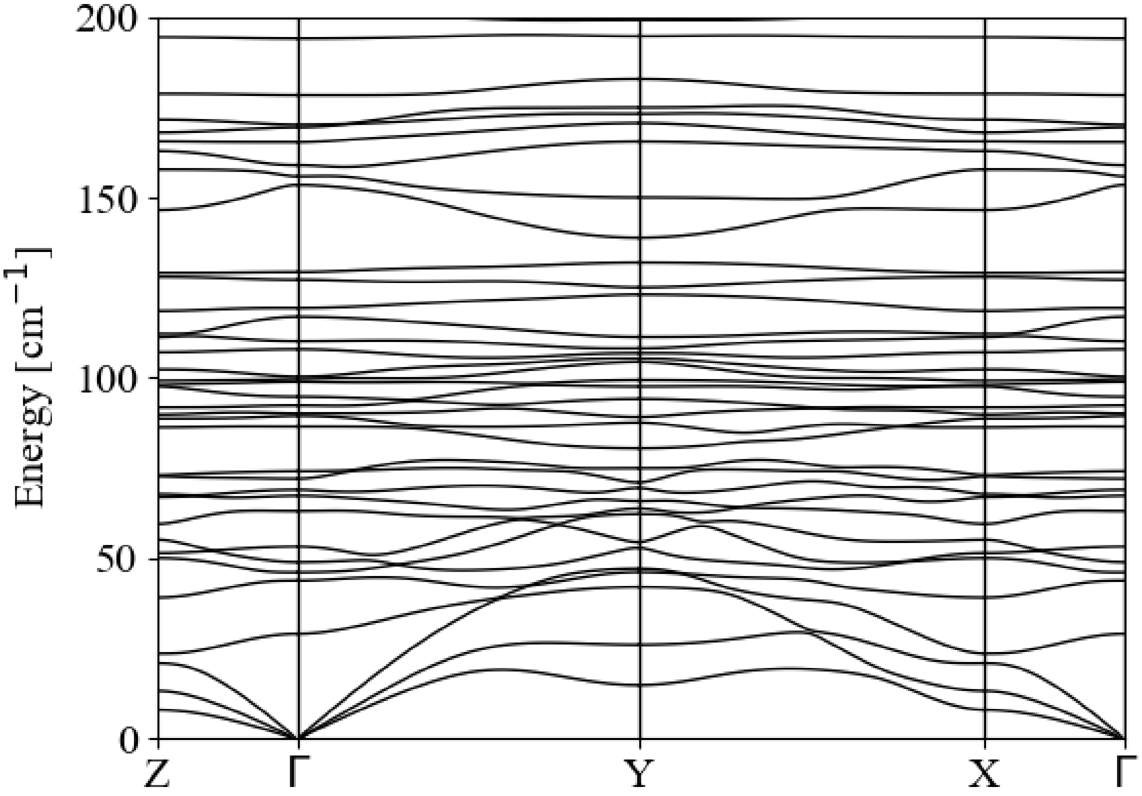

Figure S18: Phonon band structure for diF-TESADT.

References

(1) Beghi, M. G.; Bottani, C. E. Low-frequency Raman and Brillouin spectroscopy from graphite, diamond and diamond-like carbons, fullerenes and nanotubes. *Philosophical Transactions of the Royal Society A: Mathematical, Physical and Engineering Sciences* **2004**, *362*, 2513–2535.

(2) Schweicher, G.; D'Avino, G.; Ruggiero, M. T.; Harkin, D. J.; Broch, K.; Venkateshvaran, D.; Liu, G.; Richard, A.; Ruzié, C.; Armstrong, J. et al. Chasing the "Killer" Phonon Mode for the Rational Design of Low-Disorder, High-Mobility Molecular Semiconductors. *Advanced Materials* **2019**, *31*, 1902407.

(3) Zhang, Y.; Manke, D. R.; Sharifzadeh, S.; Briseno, A. L.; Ramasubramaniam, A.; Koski, K. J. The elastic constants of rubrene determined by Brillouin scattering and density functional theory. *Applied Physics Letters* **2017**, *110*, 071903.

(4) Kresse, G.; Furthmüller, J. Efficiency of ab-initio total energy calculations for metals and semiconductors using a plane-wave basis set. *Computational Materials Science* **1996**, *6*, 15–50.

(5) Kresse, G.; Furthmüller, J. Efficient iterative schemes for ab initio total-energy calculations using a plane-wave basis set. *Physical Review B* **1996**, *54*, 11169–11186.

(6) Joubert, D.; Kresse, G. From ultrasoft pseudopotentials to the projector augmented-wave method. *Physical Review B - Condensed Matter and Materials Physics* **1999**, *59*, 1758–1775.

(7) Klimeš, J.; Bowler, D. R.; Michaelides, A. Chemical accuracy for the van der Waals density functional. *Journal of Physics Condensed Matter* **2010**, *22*.

(8) Klime, J.; Bowler, D. R.; Michaelides, A. Van der Waals density functionals applied to solids. *Physical Review B - Condensed Matter and Materials Physics* **2011**, *83*, 1–13.

(9) Dion, M.; Rydberg, H.; Schröder, E.; Langreth, D. C.; Lundqvist, B. I. Van der Waals density functional for general geometries. *Physical Review Letters* **2004**, *92*, 22–25.

(10) Anthony, J. E.; Brooks, J. S.; Eaton, D. L.; Parkin, S. R.; May, R. V. Functionalized Pentacene: Improved Electronic Properties from Control of Solid-State Order. **2001**, *222*, 1–2.

(11) Payne, M. M.; Parkin, S. R.; Anthony, J. E.; Kuo, C. C.; Jackson, T. N. Organic field-effect transistors from solution-deposited functionalized acenes with mobilities as high as 1 cm2/V·s. *Journal of the American Chemical Society* **2005**, *127*, 4986–4987.

(12) Vyas, V. S.; Gutzler, R.; Nuss, J.; Kern, K.; Lotsch, B. V. Optical gap in herringbone and π-stacked crystals of [1]benzothieno[3,2-b]benzothiophene and its brominated derivative. *CrystEngComm* **2014**, *16*, 7389–7392.

(13) Izawa, T.; Miyazaki, E.; Takimiya, K. Molecular Ordering of High-Performance Soluble Molecular Semiconductors and Re-evaluation of Their Field-Effect Transistor Characteristics. *Advanced materials.* **2008-09-17**, *20*.

(14) Jurchescu, O. D.; Meetsma, A.; Palstra, T. T. M. Low-temperature structure of rubrene single crystals grown by vapor transport. *Acta Crystallogr B.* **2006**, *62*, 330–334.

(15) Togo, A.; Tanaka, I. First principles phonon calculations in materials science. *Scripta Materialia* **2015**, *108*, 1–5.

(16) Ramirez-Cuesta, A. J. aCLIMAX 4.0.1, the new version of the software for analyzing and interpreting INS spectra. *Computer Physics Communications* **2004**, *157*, 226–238.

(17) Porezag, D.; Pederson, M. R. Infrared intensities and Raman-scattering activities within density-functional theory. *Physical Review B - Condensed Matter and Materials Physics* **1996**, *54*, 7830–7836.

(18) Fonari, A.; Stauffer, S. *vasp_raman.py*; https://github.com/raman_sc/VASP/, 2013.

(19) Skelton, J. M.; Burton, L. A.; Jackson, A. J.; Oba, F.; Parker, S. C.; Walsh, A. Lattice dynamics of the tin sulphides SnS2, SnS and Sn2S3: Vibrational spectra and thermal transport. *Physical Chemistry Chemical Physics* **2017**, *19*, 12452–12465.

(20) Nematiaram, T.; Padula, D.; Landi, A.; Troisi, A. On the Largest Possible Mobility of Molecular Semiconductors and How to Achieve It. *Advanced Functional Materials* **2020**, *30*, 1–10.

(21) Nematiaram, T.; Troisi, A. Strategies to reduce the dynamic disorder in molecular semiconductors. *Materials Horizons* **2020**, *7*, 2922–2928.

(22) Frisch, M. J.; Trucks, G. W.; Schlegel, H. B.; Scuseria, G. E.; Robb, M. A.; Cheeseman, J. R.; Scalmani, G.; Barone, V.; Petersson, G. A.; Nakatsuji, H. et al. Gaussian˜16 Revision C.01. 2016; Gaussian Inc. Wallingford CT.

(23) Nematiaram, T.; Troisi, A. Modeling charge transport in high-mobility molecular semiconductors: Balancing electronic structure and quantum dynamics methods with the help of experiments. *Journal of Chemical Physics* **2020**, *152*, 190902.

(24) Malagoli, M.; Coropceanu, V.; Da Silva Filho, D. A.; Brédas, J. L. A multimode analysis of the gas-phase photoelectron spectra in oligoacenes. *Journal of Chemical Physics* **2004**, *120*, 7490–7496.

(25) Ren, X.; Bruzek, M. J.; Hanifi, D. A.; Schulzetenberg, A.; Wu, Y.; Kim, C. H.; Zhang, Z.; Johns, J. E.; Salleo, A.; Fratini, S. et al. Negative Isotope Effect on Field-Effect Hole Transport in Fully Substituted 13C-Rubrene. *Advanced Electronic Materials* **2017**, *3*, 1–7.

(26) D. Feinberg, S. Ciuchi, F. de Pasquale, Squeezing phenomena in interacting electron phonon systems. *Int. J. Mod. Phys. B* **1990**, *4*, 1317.

(27) Harrelson, T. F.; Dantanarayana, V.; Xie, X.; Koshnick, C.; Nai, D.; Fair, R.; Nuñez, S. A.; Thomas, A. K.; Murrey, T. L.; Hickner, M. A. et al. Direct probe of the nuclear modes limiting charge mobility in molecular semiconductors. *Materials Horizons* **2019**, *6*, 182–191.

(28) Xie, X.; Santana-Bonilla, A.; Troisi, A. Nonlocal Electron-Phonon Coupling in Prototypical Molecular Semiconductors from First Principles. *Journal of Chemical Theory and Computation* **2018**, *14*, 3752–3762.

(29) Coropceanu, V.; Sánchez-Carrera, R. S.; Paramonov, P.; Day, G. M.; Brédas, J. L. Interaction of charge carriers with lattice vibrations in organic molecular semiconductors: Naphthalene as a case study. *Journal of Physical Chemistry C* **2009**, *113*, 4679–4686.

(30) Fratini, S.; Mayou, D.; Ciuchi, S. The Transient Localization Scenario for Charge Transport in Crystalline Organic Materials. **2016**, *26*, 2292–2315.

(31) Fratini, S.; Ciuchi, S. On dynamical localization corrections to band transport. *arXiv* **2019**, *013001*, 1–14.

(32) Giannini, S.; Carof, A.; Ellis, M.; Yang, H.; Ziogos, O. G.; Ghosh, S.; Blumberger, J. Quantum localization and delocalization of charge carriers in organic semiconducting crystals. *Nature Communications* **2019**, *10*, 1–12.

(33) Fratini, S.; Ciuchi, S.; Mayou, D.; De Laissardière, G. T.; Troisi, A. A map of high-mobility molecular semiconductors. *Nature Materials* **2017**, *16*, 998–1002.

(34) Nematiaram, T.; Ciuchi, S.; Xie, X.; Fratini, S.; Troisi, A. Practical Computation of the Charge Mobility in Molecular Semiconductors Using Transient Localization Theory. *Journal of Physical Chemistry C* **2019**, *123*, 6989–6997.